Insight into the plasma structure of the Quad Confinement Thruster using electron kinetic modelling

Rhys David Williams[a,*], Andrea Lucca Fabris[b], Aaron Knoll[a]

[a] *Department of Aeronautics, Imperial College London, Exhibition Road, London, United Kingdom, SW7 2AZ*
[b] *Surrey Space Centre, University of Surrey, Guildford, U.K*

Abstract

The behaviour of plasma within the discharge channel of the Quad Confinement Thruster is studied on the basis of electron kinetics. Here we propose that $E \times B$ drift of electrons drives the formation of unusual quadrant dependent light emitting structures observed experimentally in the discharge channel of the Quad Confinement Thruster. This assertion is made on the basis of a theory-based analysis and a computational model of the Quad Confinement Thruster. A particle orbit model of electron motion under the influence of applied electric and magnetic fields was used to assess electron transport. Structures strongly resembling that of the observed visible emission regions were found in the electron density distribution within the channel. While the motion of electrons cannot be decoupled from the motion of ions, as in this simple electron kinetic approximation, the results of this analysis strongly indicate the physical mechanism governing the formation of the non-uniform density distributions within the Quad Confinement Thruster channel.

Keywords: Electric propulsion, Quad Confinement Thruster, $E \times B$ transport, Electron kinetic modelling

Nomenclature

B	Magnetic field
E	Electric field
m_i	mass of particle i
q_i	Charge of particle i
V_i	Velocity of particle i
$\dot{n}_{e,ref}$	reference electron number density flux
$\dot{n}_e$	electron number density flux
Γ	Electron flux at inflow boundary
μ_0	Vacuum permeability
ω_c	cyclotron frequency

*Corresponding author
Email address: a.knoll@imperial.ac.uk (Aaron Knoll)

e	Charge of the electron
I_i	Line current of line i
m_e	electron rest mass
N	Number of particles in computational domain
n_e	electron number density
$n_{e,ref}$	reference electron number density
r_c	cyclotron radius
$V_{E\times B}$	electron $E \times B$ velocity
$V_\perp$	electron non-axial velocity component
FEMM	Finite Element Method Magnetics
HET	Hall Effect thruster
PIC	Partcile in cell model
QTC	Quad Confinement Thruster

1. Introduction

The Quad Confinement Thruster (QCT), shown in Figure 1 and 2, is an Electric Propulsion (EP) device with the unique ability to provide vectored thrust without the need for any moving parts. The QCT was developed in 2010 at the Surrey Space Centre (SCC) and since then it has seen increasing interest from industry, being developed into flight hardware and launched on the Satellite Technology Ltd (SSTL) NovarSar-1 mission in September 2018 [1].

The operation of the QCT is in many ways similar to that of a linear-channel open-electron-drift Hall Effect Thruster (HET) [2]. The device consists of a metallic anode at the base of a square ceramic discharge channel with a hollow cathode mounted downstream of the channel exit. A quadrupole magnetic field is imposed in the discharge channel and acts to impede the electron mobility towards the anode. This sets up an axial electric field that accelerates the ions out of the channel producing thrust. The ion beam is then neutralised by electrons produced by the hollow cathode.

Yet to be understood, but vital to the performance of the QCT is the behaviour of the plasma in the discharge channel. A unique feature of the discharge channel is the appearance of bright visible light emitting structures that are confined to two out of the four quadrants [3]. What these structures are exactly and the physics driving their formation is so far unexplained and its impact on the thruster unknown.

In this paper we model the plasma assuming free motion of electrons in externally applied electric and magnetic fields without modelling internal self consistent fields. We then infer the plasma properties from the electron distributions.

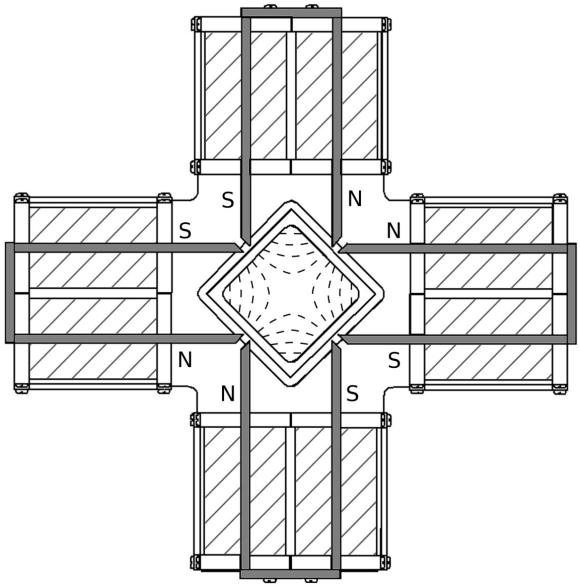

Figure 1: Front on drawing of the Quad Confinement thruster showing magnetic design. Electromagnets are hatched, iron core's highlighted in solid grey, the channel bound magnetic field is shown as dashed lines, and the poles are marked as north (N) and south (S)

2. Overview of the QCT

2.1. Operation and performance of the QCT

A cross section of the QCT is shown in figure 2. The thruster consists of a square cross sectioned discharge channel, which is constructed of boron nitride ceramic with dimensions 30 × 30 × 55 mm [4]. Xenon propellent gas is introduced at the rear of the channel at the location of a square cross sectioned anode. The QCT utilises four electromagnets, one at each corner of the discharge channel, to impose a magnetic field that extends the length of the channel. The channel in-plane magnetic field has a quadrupole structure, the topology is shown in figure 1.The strength and shape of the magnetic field is relatively constant throughout the axial extent of the discharge channel [4]. A hollow cathode is located downstream of the channel exit plain and is used as a source of primary electrons for plasma generation and neutralisation of the ion beam.

The structure of the magnetic field within the QCT channel acts to weakly confine the electrons, leading to the formation of plasma in the discharge channel. The low axial mobility of electrons sets up an axial electric field within the plasma. Xenon ions, owing to their high mass to charge ratio, are virtually unaffected by the magnetic field and are accelerated axially by the electric field to the channel exit producing thrust.

One of the unique features of this device is that the QCT is able to steer the ion beam by asymmetrically powering the four electromagnets. It has been observed through mapping the ion velocity field [3] that the ion beam can be steered 15 deg off the thruster axis by asymmetrically powering the four electromagnets.

Thrust measurements were made in previous experiments using an inverted pendulum thrust stand. The thrust stand displaces horizontally in response to an applied force, with the displacement measured using a high precision laser triangulation sensor, see [4] for full details of thruster performance experiments. A maximum thrust of 3.2 mN has been observed for a anode flow rate of 6 sccm and 200 W anode power. Giving a power to thrust ratio of 63 W/mN. The specific impulse of the thruster is calculated based on measured thrust normalised by anode flow rate. This gives a specific impulse at maximum thrust of approximately

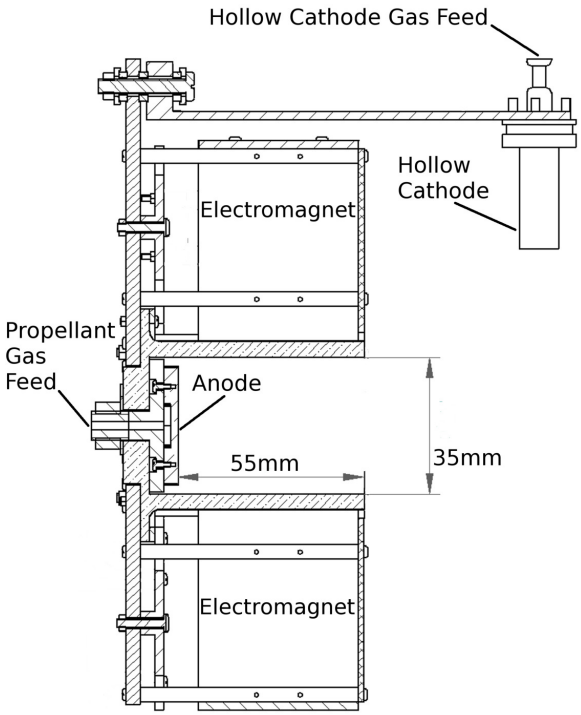

Figure 2: Side on cut through symmetry line drawing of the Quad Condiment Thrust

520 s. The maximum observed specific impulse of the QCT is 860 s at a 2 sccm flow rate. Thrust efficiency is calculated as the kinetic energy of the outgoing ion beam normalised by anode power. A maximum thrust efficiency of the QCT of approximately 4% is observed when the magnetic field has a strength of 250 Gauss [4]. It has been noted however that the thrust efficiency increases rapidly with magnetic field strength and that the maximum value has not yet been identified for the QCT.

2.2. Experimental observations

Photographs of the discharge region taken at the European Space Agency Electric Propulsion Laboratory (Shown in Figure 3 (a) and (b)) indicate a non-uniformity in the distribution of plasma within the discharge channel, and downstream of the channel exit: a dual lobed structure inside and a semi-spherical structure outside the channel. The side view (Figure 3 (b)) shows that the lobed structure very quickly gives way to the semi-spherical structure at the exit of the channel.

Two spectral lines dominate visible light emissions in Xe plasma's and give rise to their characteristic blue glow seen in the photographs [5, 6]. The typically weaker line is associated with Xe I at 467.1 nm and the stronger with Xe II 484.4 nm [7, 5]. The emission spectra of Xe in HET's is well studied and has been catalogued elsewhere [6].

Light is produced by radiative relaxation consequent to collisional excitation events therefore the emission intensity is dependent on electron density, Xe species density and collisional excitation rates [5]. Therefore, in areas of high electron number density we may expect higher intensity visible emissions. This is however complicated by the existence of metastable excited states [5]. States of Xe I that can decay producing visible light may exist in an excited state up to lifetimes on the order of seconds [8, 9]. This makes it possible for

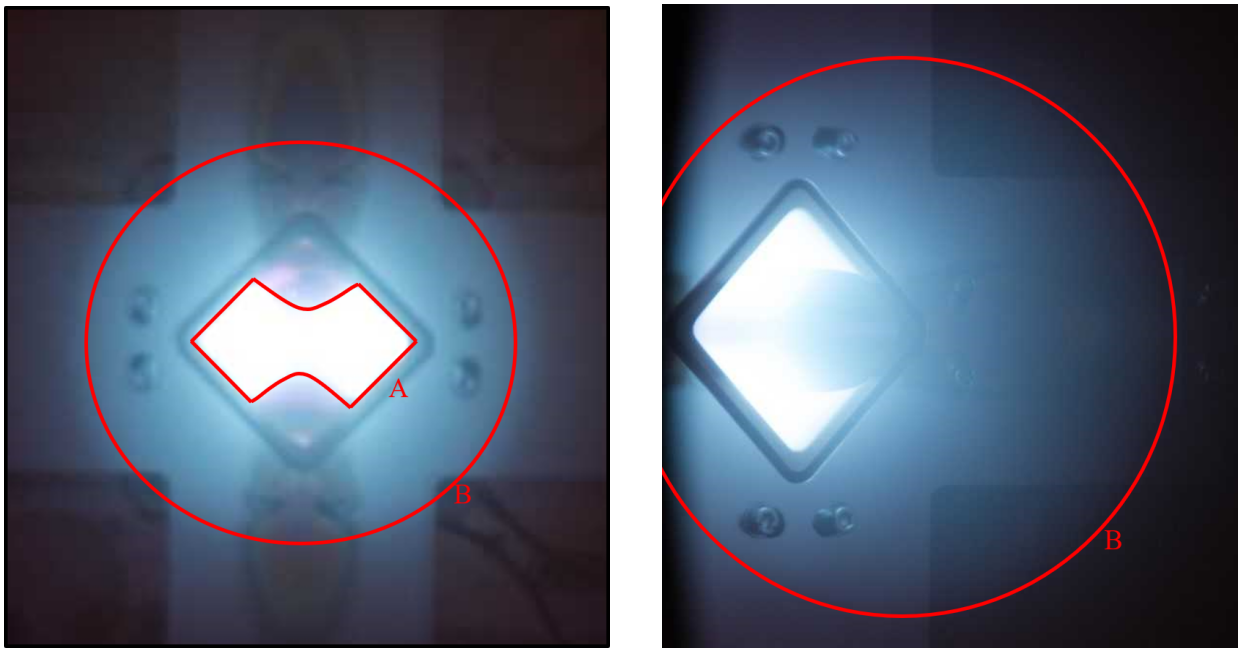

Figure 3: Direct look down the channel (a) and side on view (b) of the QCT in operation. The channel light emitting region is labelled A and the external semi-spherical region B. The boundaries of the structures are highlighted in red.

a metastable state to migrate to a different region of the channel before emitting a visible photon. This mechanism is partly responsible for the so-called afterglow effect seen in some plasma devices [10].

2.3. Empirical and theoretical considerations

It has been observed experimentally that the increase in background pressure in the test chamber during operation of the QCT led to a smearing of the light emitting structures, up until the point they filled the entire channel. This indicates that an increased number density of neutrals tends to disrupt the formation of the organised emission structure. Background neutrals influence the plasma primarily through non Coulomb collisional effects.

2.4. Correlation with electric and magnetic field structure

Laser Induced Fluorescence measurement of the ion velocity indicates that little ion acceleration takes place in the discharge channel relative to the downstream acceleration front [3]. From the plasma potential [11] and the ion axial velocity distribution [3] seen experimentally we expect the axial electric field to be radially uniform with a value of ≈ 260 V/m, pointing away from the anode.

If we compare the applied magnetic field with the visible emission structure shown in Figure 4 we find a strong correlation between the field structure and the visible emission regions. This suggests that the structure and direction of the magnetic field in the channel may be contributing to the formation of the emission structures. This is further supported by the fact that flipping the field direction was noted to switch the quadrants in which visible emission was observed.

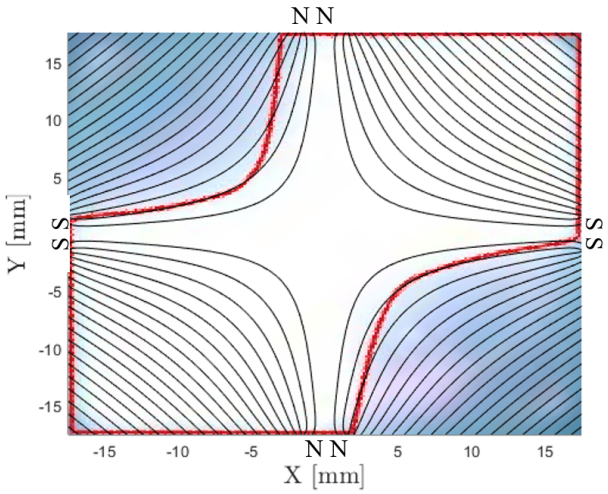

Figure 4: Discharge channel magnetic field line structure generated in FEMM [12] overlaid with photo of the channel light emission region. The boundary of the light emission is highlighted (red) and the magnetic poles are labelled north (N) and south (S).

The visible emission structures clearly appears to follow the magnetic field lines. The non-uniformity of the plasma and quadrant dependant behaviour points to the action of the $E \times B$ transport of electrons. To evaluate this predicted $E \times B$ drift directions were produced and compared to the emissions, see Figure 5.

There is a strong correlation between the $E \times B$ drift directions and the emission regions. Emission regions appear to be correlated with the cross drift directions towards the channel walls, and the dark regions with cross drift directions away from the channel walls.

2.5. Magnetisation of the plasma species

In order for the $E \times B$ drift to act on charged particles within the plasma directly they must be magnetised. We can impose two conditions which must be satisfied in order to determine if a species is magnetised [13]. Condition one states that the species must be able to carry out many cyclotron orbits before encountering a boundary of the system. This implies that the cyclotron radius (r_c) is far less than the characteristic size of the system L, $\frac{L}{r_c} \gg 1$. Condition two states that the charges must also be able to undergo many cyclotron orbits before being disrupted by a collision with a neutral atom.

We first confirm whether the electrons and major ion species within the QCT plasma satisfy these constraints. For the electrons we estimate their average velocity of 1.339×10^6 m/s from the mean velocity for a population with a temperature of 4 eV assuming a Maxwell Boltzmann distribution. The Xe II species is the least magnetisable and most populous of the ion species in the plasma. To study it we will use the axial velocity found from experimental data at the channel exit plain, using a approximate ion velocity of 1.5×10^3 m/s [3]. The characteristic length of the QCT system for the purposes of wall collisions is taken to be the width of the channel that 35 mm.

For the Xe II species at the peak magnetic field strength in the channel of 250 Gauss, $\frac{L}{r_c}$ is found to be 0.43, far from satisfying condition one.

Examining the electrons, $\frac{L}{r_c}$ is found to be 115 at the peak field strength. We must acknowledge that the magnetic field strength in the QCT varies substantially in the discharge channel, dropping to 0 at the centre. There is always a region at the centre of the channel where the electrons are not magnetised. Making the broad assumption that electrons are not strongly magnetised for $\frac{L}{r_c}$ values less than 10, it is found that the non-magnetised region is insubstantial (< 1 mm across) for electrons with velocity up to mean velocity.

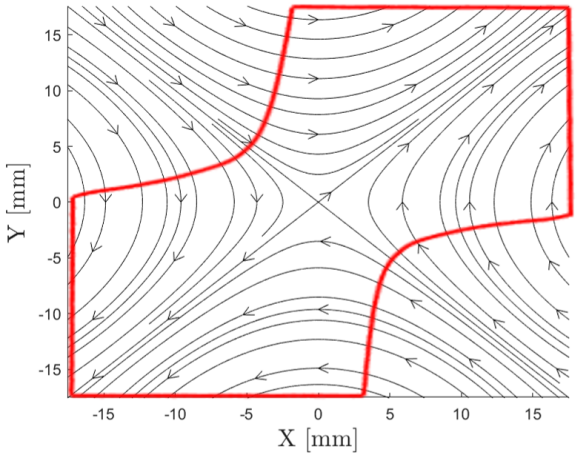

Figure 5: Direction of the $E \times B$ drifts in the channel of the QCT. Generated from the magnetic field outputted by FEMM and the electric field approximated from experimental observations. The location of the boundary of the channel emission structure observed experimentally is highlighted in red

Typical values for electron-neutral collision frequencies for hall effect thruster plasma's are found to be of order 10^6 1/s [14], and the cyclotron frequency (ω_c) for the electron in these conditions is of order 10^9 1/s. Given the similarity in the neutral density, electron temperature, and magnetic field strength between the HET and QCT, we expect these conditions to be similar for the QCT discharge.Therefor, neutral collision do not result in demagnetised electrons.

We may summarise for the electrons that the majority of the population are magnetized across all but a small region at the centre of the channel, with the size of this region growing for high energy electrons. The electrons will therefore be driven by the $E \times B$ drift.

As the Xenon species are not magnetised a charge space difference will undoubtedly develop in the plasma as a result of electrons drifting away from the ions in the $E \times B$ drift. We therefore expect ambipolar diffusion to be important for the collective movement of electrons and ions within the channel.

2.6. Proposed Mechanism

The proposed mechanism for the formation of the light emitting structures is the transport of highly magnetised electrons in $E \times B$ drifts coupled to the transport of ions by ambipolar diffusion. As the electrons enter the channel they become highly magnetised and begin to experience $E \times B$ drifts. The direction of the $E \times B$ drifts lead's to a depletion or concentration of electrons in the quadrants where the drift points away and towards the walls respectively.

The higher number density of electrons in two of the quadrants will lead to an enhanced number of ionisation events. Consequently, more plasma will form in the higher electron concentration quadrants. Secondary electrons produced in ionisation events will also tend to be concentrated by the $E \times B$ drifts.

The xenon ion species in the plasma are not highly magnetised and are instead concentrated into the same regions as the electrons by the action of ambipolar diffusion. Ambipolar diffusion will act to slow the collective motion of the electrons and increase the transport of the ions so as to preserve charge neutrality.

Once a plasma structure has formed in the quadrants it will tend to be confined there due to magnetic field lines which bound each quadrant. The effect of collisions with neutrals will tend to disrupt the concentration by interrupting cyclotron orbits and hence reducing the intensity of the $E \times B$ drifts.

The net effect of the mechanism described will be the higher number density of ions and electrons within two of the four quadrants leading to a greater production of excited states of xenon. These states may then decay producing visible light in the manner observed experimentally.

3. Numerical Model

3.1. Model selection

For the computational investigation of the QCT plasma a discrete electron transport model was built in MATLAB that is able to model the motion of many independent discrete charges, with random initial electron states. The key limitations of this approach versus full particle-in-cell simulations [15, 16] is that electric fields cannot be self-consistently captured, and must be imposed using simple assumptions or experimental measurements. Despite this lack of fidelity, computations can be performed at vastly larger length and time scales as they do not need to meet the constraints of Debye length or plasma frequency. The lower computational cost of these models will allow us to simulate the entire QCT channel. This will enable the study of the full formation and propagation of structures in the QCT which will be necessary to test the predicted mechanism. Other studies have had substantial success in predicting the properties of plasma in Hall Effect thrusters and other devices using these simpler models [17, 18, 19].

3.2. Model assumptions

The general governing equations for the model are based on the Lorentz force acting on some particle i at some time t:

$$\frac{\mathrm{d}v(t)_i}{\mathrm{d}t} = \frac{q_i}{m_i}(E(t)_i + v(t)_i \times B(t)_i) \tag{1}$$

$$\frac{\mathrm{d}x(t)_i}{\mathrm{d}t} = v(t)_i \tag{2}$$

We make the following simplifying assumptions in building the computational model:

1. Electron motion is dominant in determining the 3-D structure of the plasma as a result of being the only magnetised species. Consequently only electrons are modelled. This allows us to reduce the degrees of freedom of (1) by letting $\frac{q_i}{m_i} = \frac{e}{m_e}$ for all particles where $\frac{e}{m_e}$ is the mass to charge ratio of the electron.
2. The motion of the electrons is primarily determined by the externally applied fields. We justify this on the basis of our theoretical analysis in Section 3. We exploit the assumption in order to neglect internal fields from the model, only allowing applied fields to act on the charges. This decouples the motion of each electron. As a result the model is not self-consistent. Collisions with neutral species or with other electrons are neglected. We do however model elastic scattering events at the channel walls.
3. The external fields are assumed to be constant in time with the electric field constant in space, allowing us to drop the spatial and time dependence of the field from (1). Spatial variation is allowed in the cross channel direction of the magnetic field, the magnetic field strength is constant down the channel
4. A constant, randomly spatially distributed, inflow of electrons into a pre-channel region is assumed. The populations velocities are determined by a Maxwell Boltzmann distribution.
5. Sheath effects at the anode and channel walls are neglected.

3.3. Implementation

The commonly used Boris algorithm [20] was selected for the particle advancement. It is second order accurate and time centred, and has a large advantage over other time stepping algorithms in the fact that it is energy conserving. This places a global bound on numerical error when using the algorithm [21].

In defining the magnetic field in the domain, we opt to model the field using a set of infinite line. Such an analytic approach is preferred over extracting the field solution from a mesh, for instance from a Finite Element Model, because it results in a smooth field without any discontinuities across mesh boundaries. The accurate tracking of the field lines by the gyration centres of particles is important in classical motion, making proper representation of field curvature important. This is exacerbated the more finely we wish to resolve electron motion using small time steps. In order to resolve this, we construct a field that is very close to the true QCT field using a set of infinite line currents. This allows us to define a smooth analytic expression for the magnetic field at all locations in the domain. The field is defined to be a constant strength axially in the channel, justified by experimental observations of a close to constant field strength along the channel axis [4]. To ensure line current singularities do not affect the model the line currents are set at some standoff distance from the domain. The equation for the magnetic field produced by the line current is defined in equation 3:

$$(B_x, B_y) = \frac{\mu_0}{2\pi} \sum_{i=1}^{8} I_i \frac{(y_i - y, x - x_i)}{(x - x_i)^2 + (y - y_i)^2} \tag{3}$$

Where x_i and y_i are defined relative to the central of the channel. The values used in the model are summarised in table 1.

Table 1: Line current model settings, $I = 8 \times 10^4$ A, $L = 35 \times 10^{-3}$ m is the channel width, $D_{set} = 35 \times 10^{-3}$ m is the offset from the channel walls, $a = 0.4$ scales where along the channel walls the line current is placed.

Index i	I_i **[A]**	x_i **[m]**	y_i **[m]**
1	I	$-(L + D_{set})$	$-(1 - a)L$
2	I	$-(1 - a)L$	$-(L + D_{set})$
3	-I	$(1 - a)L$	$-(L + D_{set})$
4	-I	$L + D_{set}$	$-(1 - a)L$
5	I	$L + D_{set}$	$(1 - a)L$
6	I	$(1 - a)L$	$L + D_{set}$
7	-I	$-(1 - a)L$	$L + D_{set}$
8	-I	$-(L + D_{set})$	$(1 - a)L$

The computational domain is setup as follows:

$$x \in (0, L) \quad y \in (0, L) \quad z \in (0, L_{ax}) \tag{4}$$

The particles are subject to the following boundary conditions:

$$x = 0 \quad \text{or} \quad L, \quad y = 0 \quad \text{or} \quad L \quad \text{Elastic scattering} \tag{5}$$

$$z = 0, \quad \Gamma_e = \alpha \quad z = L_{ax}, \quad \text{Particle is deleted} \tag{6}$$

Where α sets some electron flux at the inflow boundary, for our model we set this to 4.058×10^{15} $1/\text{m}^2/\text{s}$. Applied external fields are modelled as:

$$B = \left\{ \begin{array}{c} [0, 0, 0]^T \text{ z} \in (0, L_{ax} - L_{channel}) \\ [B_x, B_y, 0]^T \text{ z} \in (L_{ax} - L_{channel}, L_{ax}) \end{array} \right\}$$

$$\mathrm{E} = [0,0,\mathrm{E}_{ax}]^T$$

A 1 cm long pre-channel region with only an electric field acting was setup in the domain. This region acts as a control in order to study the behaviour of the electrons with and without the magnetic field, allowing us to distinguish $E \times B$ related behaviour.

For resolving the electron motion we must select a time step smaller than the smallest cyclotron period in the plasma. We calculate this minimum cyclotron period of 1.42×10^{-9} s at a peak field of 250 Gauss. In order to resolve the full cyclotron orbit for the most energetic electrons we therefore select a time step of 1×10^{-10} s. As for a PIC method the amplitude of the noise in the simulation scales with the number of particles [22] N as Noise $\propto N^{-0.5}$. The computational demand however scales with N, therefore we must find a compromise between run time and computational noise. The number of electrons in the simulation domain fluctuates over time as a balance of the inflow and outflow from the channel, it however settles to a near steady value of 5×10^6.

The initial electron velocity distribution was calculated for an electron temperature of 4 eV to match experiment. The electric field is set to be purely axial out of the channel with a value of $\approx$ 260 V/m. The magnetic field is set at a peak field of 261 Gauss and average field of 156 Gauss to match experimental values. The simulation was run till a steady state electron distribution was reached, approximately 1×10^{-7} s.

4. Results

4.1. Density maps

Figure 6 show maps of the normalised number density distributions at four axial stations, 5, 10, 11.5 and 27.2 mm within the simulation domain. The densities are normalised with respect to the inflow plain.

We see in the upstream control region (Figure 6 (a)) that the electron densities are homogenous. However, at the point the magnetic field begins to act we see an immediate concentration of the electrons into the quadrants that correspond to the bright emission regions.

The structure of the electron density in the divergence region plotted in Figure 6 (b) and (c) shows a striking resemblance to the shape of the observed visible emission. This is compelling evidence that the bright emission regions arise as a result of increased electron density formed under the action of the proposed mechanism. We observe in the central region a set of circular concentric structures of increased electron densities compared to the background. This is expected due to the prediction of demagnetised electrons that are transported in plane purely through random thermal motion. Indeed, the size of the circles resembles that of the demagnetised zones for electrons with a standard deviation more energy than the mean.

As the structure further develops within the channel (Figure 6 (d)) there is a notable drop in the densities near the side walls. The electrons appear to be confined to two central bundles in the light emitting quadrants. It is likely that wall collisions are enhancing axial electron mobility by disrupting cyclotron orbits. In these regions the electron mobility is increased in the axial direction die to wall collisions and rapidly escape the simulation domain. We also see the central regions have been depleted of electrons.

4.2. Axial electron density distribution

Figure 7 shows the normalised electron number densities down the length of the channel. The number of electrons in the simulation was selected to provide an acceptable signal to noise ratio of 42 dB. The number densities presented are for the quadrants where light emitting structures have been observed experimentally, labelled bright quadrants, and where no light emission is observed, labelled dark quadrants. The number densities are normalised relative to a reference upstream condition.

The general behaviour of the electrons can be split into three regions; the control region (z = 0 m to 0.01 m), characterised by spatially uniform, axially decreasing number density of electrons. The divergence

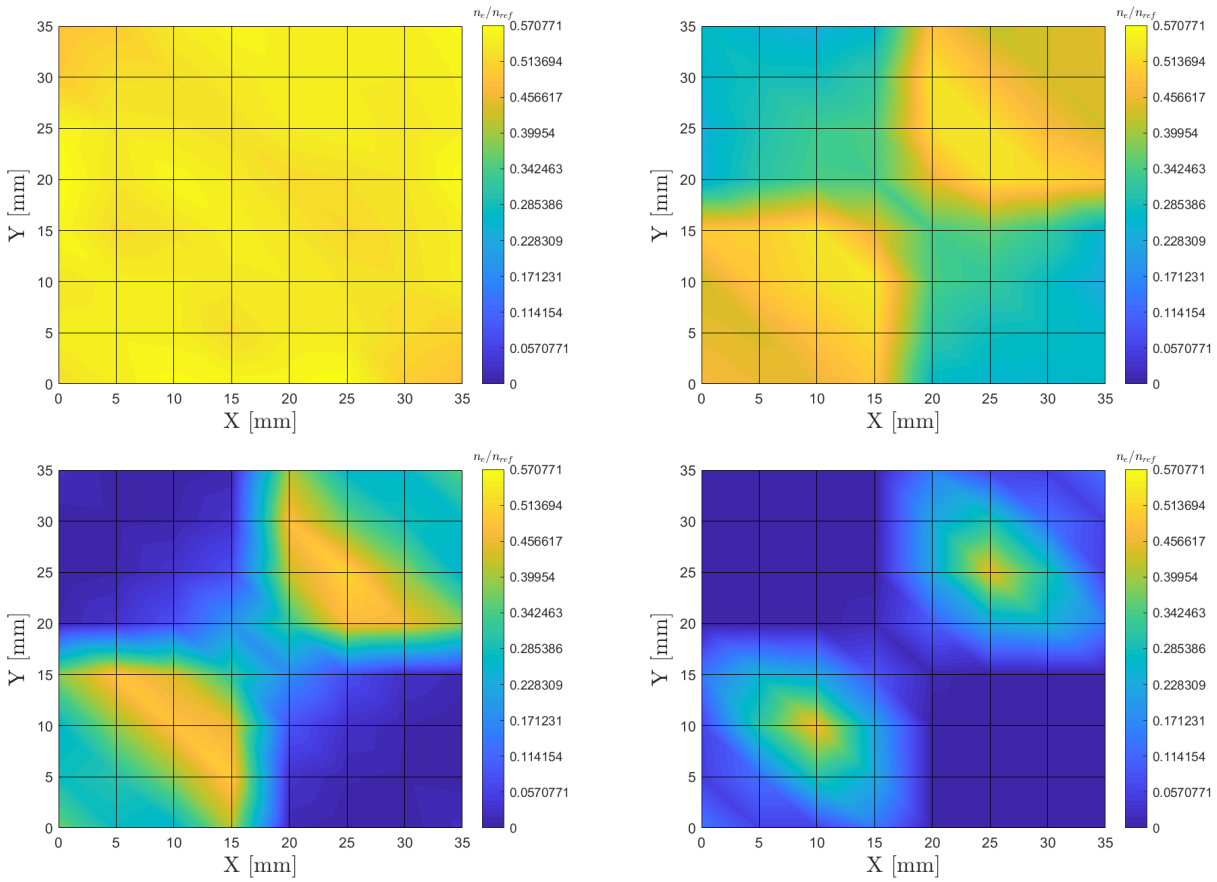

Figure 6: Normalised electron density maps. At an axial location upstream of the channel entrance with a Z value of 5 mm (a), and downstream of the channel entrance at Z values of 10 mm (b), 11.5 mm (c), and 27.2 mm (d).

region (z = 0.01 m to 0.015 m), where electron densities rapidly change in quadrants and divergence takes place between the bright and dark quadrants. Finally the post divergence region (from z = 0.015 m) where the electron density declines at a slower, more steady rate.

In the control region upstream of the channel entrance, where only an axial electric field is present we observe an approximately constant decrease in electron number density. This is an expected result that corresponds to the axial acceleration of the electrons. Importantly in this control region the bright and dark quadrants are relatively close in density.

At the point of entering the channel where the magnetic field is applied we see an immediate divergence of the number densities. Comparing to the control region we can state that this is the action of the channel magnetic field. After this divergence region we see the electron number density decrease at a slower steady rate in the bright quadrants, and remain near zero in the dark quadrants. It is interesting to note that the electron density drops more rapidly in the magnetised versus unmagnetized (control) section of the channel. This somewhat counterintuitive result indicates that the structure of the magnetic field increases the axial electron mobility.

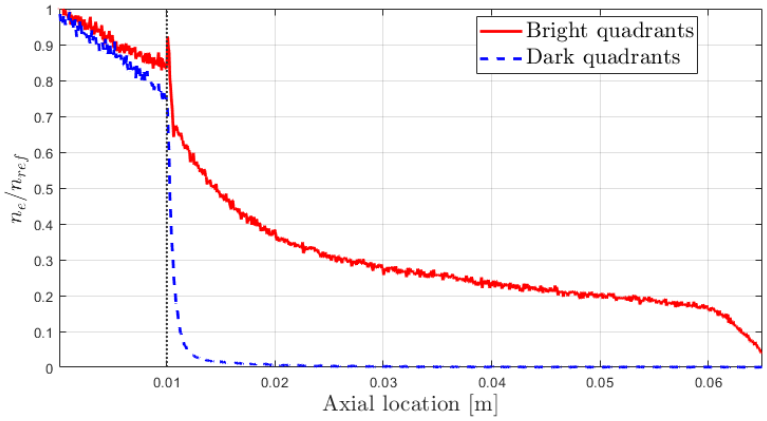

Figure 7: Normalised average electron number densities along the discharge channel, the start of the channel and hence the start of action of the magnetic field is marked by a dashed line. The number density for the quadrants where light emission is observed experimentally is plotted in red, and where no light emission is observed in blue. The electrons are flowing from left to right.

4.3. Axial mobility

The normalised axial electron number density flow rate $\dot{n}_e/\dot{n}_{ref}$ maps at different axial locations in the channel are shown in Figure 8.

Examining Figure 8 (a) there is no clear structure to the axial electron flow distribution in the control region. When the magnetic field ((b) to (d)) is applied we see the formation of a bright central region with higher axial mobility electrons. This region corresponds well with the predicted region of demagnetised electrons.

There is no correlation between the axial mobility maps and the regions of bright emission. Indicating no link between the axial movement of the electrons and the emission regions.

This behaviour does however offer an explanation for the sudden drop in electron number densities observed in the divergence region of Figure 7. As the magnetic field is applied the electrons are circulated in the channel and begin to concentrate into the emission quadrants, during this process many of the electrons pass into this high mobility region and are transported down the channel, leading to rapid electron depletion. Once the emission structures have formed there is relatively little electron circulation into the central region and the electron number densities become more stable as indicated by the slower depletion in the post divergence regions.

4.4. Electron energies

Two generally representative maps of the electron energies from the control and divergence region can be seen in Figure 9 (a) and (b) respectively.

Examining the maps of electron energy, there appears to be no clear structure either in or during the divergence region. This suggests that a difference in electron energies between the quadrants is not a driver in the production of the light emitting regions.

4.5. $E \times B$ velocity

In order to assess the importance of the $E \times B$ drift in the formation of electron density structures, maps where produced of the component of electron velocities in $E \times B$ direction ($V_{E\times B}$) normalised by

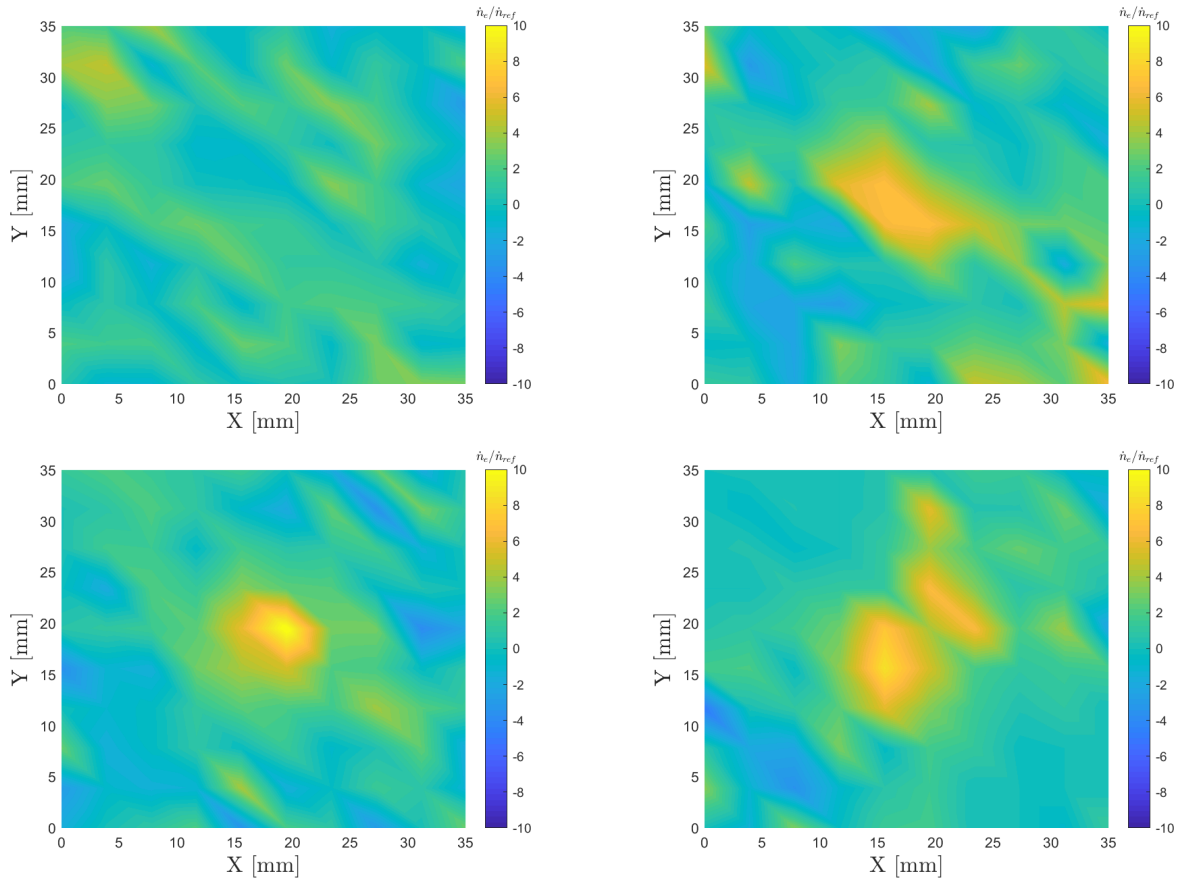

Figure 8: Normalised axial number density flow rate maps. At an axial location upstream of the channel entrance with a z value of 5 mm (a), and downstream of the channel entrance at z values of 10 mm (b), 11.5 mm (c), and 27.2 mm (d).

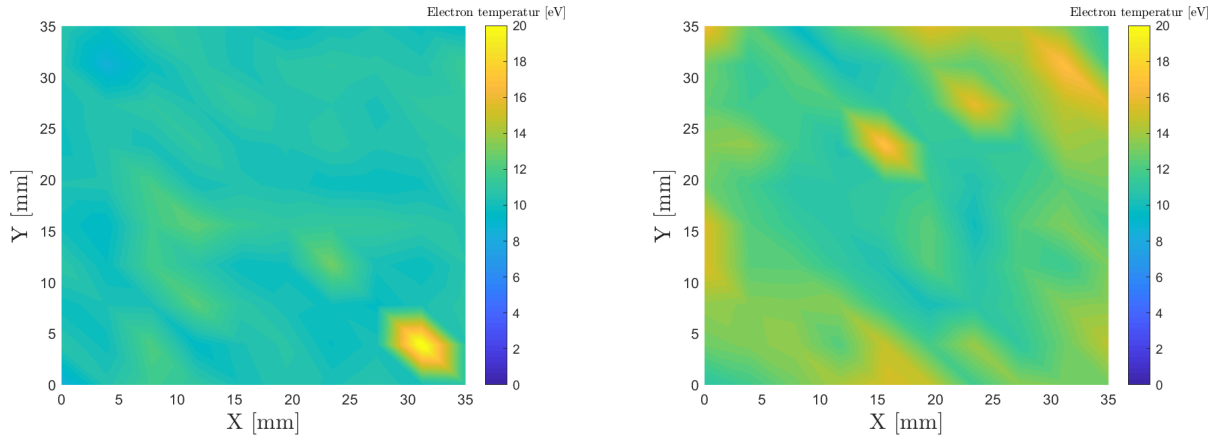

Figure 9: Electron temperature in eV maps upstream of the channel entrance (z = 5 mm) (a), and downstream of the channel entrance (z = 10.5mm) (b).

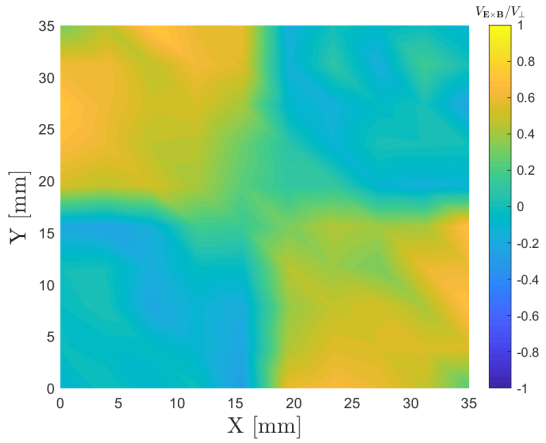

Figure 10: Component of in x-y plane velocity in local $E \times B$ direction normalised by x-y plane velocity map. Map downstream of the channel entrance (z = 10.5mm)

the non-axial component of the electron's velocity ($V_\perp$). This allows us to evaluate what proportion of the electron's in-plane motion is governed by the $E \times B$ drift.

In the divergence region shown in Figure 10 we see that the $E \times B$ is clearly driving a large amount of the in-plane electrons motions. The $V_{E\times B}$ is a dominant component of $V_\perp$ over most of the cross section, even more so in the quadrants where light emission is not observed. From our knowledge of the $E \times B$ drift directions we can state that the electrons are being rapidly driven out of the dark quadrants and then concentrated into the bright ones directly along $E \times B$ drift paths.

This result combined with the evidence presented above forms a compelling argument for the proposed mechanism of $E \times B$ action.

5. Conclusion

We have identified the possible nature and driving mechanism of the previously unexplained visible emission structures within the Quad Confinement Thruster. We propose that the $E \times B$ driven transport of electrons results in an ambipolar diffusion of plasma into two quadrants of the Quad Confinement Thruster channel, and a corresponding reduction in the density within the two remaining quadrants. This mechanism was numerically demonstrated using a simple electron kinetic model. It is hoped that this work can be used to inform design changes to the Quad Confinement Thruster in order to improve in-channel plasma behaviour. Further work is needed to validate the computational results of this study using experimental measurements of the in-channel plasma. A full particle in cell model could also be performed to assess the effect of ambipolar diffusion and collisions on the visible emissions.

References

[1] Lane O, Knoll A. Quad confinement thruster–industrialisation & flight integration. In: 34th International Electric Propulsion Conference Proceedings. 2015,.

[2] Schmidt D, Meezan N, Hargus Jr W, Cappelli M. A low-power, linear-geometry hall plasma source with an open electron-drift. Plasma Sources Science and Technology 2000;9(1):68.

[3] Lucca Fabris A, Knoll A, Young CV, Cappelli MA. Ion acceleration in a quad confinement thruster. In: Proceedings of the 35th International Electric Propulsion Conference Georgia Institute of Technology, Atlanta, Georgia, USA. IEPC CONFERENCE; 2017,.

[4] Knoll A, Harle T, Lappas V, Pollard M. Experimental performance characterization of a two-hundred-watt quad confinement thruster. Journal of Propulsion and Power 2014;30(6):1445–9.

[5] Karabadzhak GF, Chiu Yh, Dressler RA. Passive optical diagnostic of xe propelled hall thrusters. ii. collisional-radiative model. Journal of applied physics 2006;99(11):113305.

[6] Leray P, Bonnet J, Pigache D, Minea T, Bretagne J, Touzeau M. Spectroscopic emission spatially resolved along an spt channel. In: European Spacecraft Propulsion Conference; vol. 398. 1997, p. 447.

[7] Chiu Yh, Austin BL, Williams S, Dressler RA, Karabadzhak GF. Passive optical diagnostic of xe-propelled hall thrusters. i. emission cross sections. Journal of applied physics 2006;99(11):113304.

[8] Walhout M, Witte A, Rolston S. Precision measurement of the metastable 6s [3/2] 2 lifetime in xenon. Physical review letters 1994;72(18):2843.

[9] Dong C, Fritzsche S, Fricke B. Theoretical study of the 5p 5 6s–5p 6 spectra of neutral xenon. The European Physical Journal D-Atomic, Molecular, Optical and Plasma Physics 2006;40(3):317–23.

[10] Adler F, Davliatchine E, Kindel E. Comprehensive parameter study of a micro-hollow cathode discharge containing xenon. Journal of Physics D: Applied Physics 2002;35(18):2291.

[11] Knoll A, Shafiq U, Lappas V, Perren M. 3-dimensional mapping of plasma properties in the plume region of the quad confinement thruster 2012;.

[12] Meeker D. Finite element method magnetics. FEMM 2010;4:32.

[13] Hagelaar G, Oudini N. Plasma transport across magnetic field lines in low-temperature plasma sources. Plasma Physics and Controlled Fusion 2011;53(12):124032.

[14] Kaganovich I, Raitses Y, Sydorenko D, Smolyakov A. Kinetic effects in a hall thruster discharge. Physics of Plasmas 2007;14(5):057104.

[15] Dawson JM. Particle simulation of plasmas. Reviews of modern physics 1983;55(2):403.

[16] Verboncoeur JP. Particle simulation of plasmas: review and advances. Plasma Physics and Controlled Fusion 2005;47(5A):A231.

[17] Smith AW. Field structure and electron transport in the near-field of coaxial Hall thrusters. Stanford University; 2010.

[18] Smith AW, Cappelli MA. Single particle simulations of electron transport in the near-field of hall thrusters. Journal of Physics D: Applied Physics 2010;43(4):045203.

[19] Gesto FN, Blackwell BD, Charles C, Boswell RW. Ion detachment in the helicon double-layer thruster exhaust beam. Journal of propulsion and power 2006;22(1):24–30.

[20] Boris JP, Shanny RA. Proceedings: Fourth Conference on Numerical Simulation of Plasmas, November 2, 3, 1970. Naval Research Laboratory; 1972.

[21] Qin H, Zhang S, Xiao J, Liu J, Sun Y, Tang WM. Why is boris algorithm so good? Physics of Plasmas 2013;20(8):084503.

[22] Birdsall CK, Langdon AB. Plasma physics via computer simulation. CRC press; 2018.